Supporting Information

Sahli et al. 10.1073/pnas.1706434115

SI Notes

Contact Area Measurement. In digital images of multicontact interfaces (e.g., Fig. 1*B*), real contact regions appear with low gray levels whereas out-of-contact regions correspond to higher gray levels. We can thus classify the pixels using a threshold on their gray level. The threshold value is determined automatically as explained in the following.

Maximum a posteriori thresholding. The idea is to formulate the thresholding as a two-class classification problem. A given pixel can belong to class C_1 of contact pixels or to class C_2 of out-of-contact pixels and we want to assign it the best class based on its gray level z. If we can build a conditional probabilistic model giving the probability of having one class given the gray level, the classification problem can be solved using the maximum a posteriori (MAP) decision rule.

Formally, we denote $p(C_1|z)$ (respectively $p(C_2|z)$) the probability for a pixel to be in class C_1 (respectively C_2) given its gray level z. The best class assignation $\hat{k}$ is given by

$$\hat{k} = \arg \max_{k\in\{1,2\}} p(C_k|z), \qquad \text{[S1]}$$

with arg max the operator returning the argument of a function at its maximum.

In practice the posteriors $p(C_k|z)$ are not always available and Bayes' theorem is used to decompose them as

$$p(C_k|z) = \frac{p(C_k)p(z|C_k)}{p(z)}, \qquad k \in \{1,2\}.$$

The evidence term $p(z)$ being independent from the classes, Eq. **S1** can be written as

$$\hat{k} = \arg \max_{k\in\{1,2\}} p(C_k)p(z|C_k). \qquad \text{[S2]}$$

If the two conditional densities $p(z|C_k)$ (likelihoods) are unimodal, there exists a unique threshold level $\hat{z}$ such that

$$\begin{cases} p(C_1)p(z|C_1) < p(C_2)p(z|C_2) & \text{if } z < \hat{z} \\ p(C_1)p(z|C_1) \geq p(C_2)p(z|C_2) & \text{if } z \geq \hat{z} \end{cases}.$$

This threshold $\hat{z}$ is a solution of the equation

$$p(C_1)p(z|C_1) = p(C_2)p(z|C_2). \qquad \text{[S3]}$$

Probabilistic model. To find the optimal threshold, we need to model the two terms of Eq. **S3**. These terms can be estimated from the image histogram, assuming a parametric model of the two classes C_1 and C_2. Indeed, the normalized histogram $h(z)$ of gray levels of an image to be segmented is an estimation of the probability density function $p(z)$ of gray levels in this image. Given the two pixel classes, we have

$$h(z) = p(C_1)p(z|C_1) + p(C_2)p(z|C_2). \qquad \text{[S4]}$$

In Fig. S5*C*, we note the two modes of the histogram corresponding to the two terms of Eq. **S4**.

Parametric model. We choose to model each of the two classes by a parametric model inspired by the shape of the corresponding histograms. For the contact class, a Gaussian distribution is assumed,

$$G_{\mu,\sigma}(z) = \frac{1}{\sigma\sqrt{2\pi}} \exp -\frac{(z-\mu)^2}{2\sigma^2}, \qquad \text{[S5]}$$

with σ the SD of the Gaussian and μ its mean. Note that σ may include second-order nonlinear effects of light transmission through air where the two solids are separated by a gap smaller than the light's wavelength.

For the noncontact class, an empirical distribution (distorted Gaussian) was inspired by the histogram of the images completely out of contact (Fig. S5*D*). Its form is given in Eq. **S6**,

$$F_{b,c,d}(z) = a \exp \left(\frac{z-b}{c}\right)^2 \log(1 + \exp 0.1(z-d)), \qquad \text{[S6]}$$

with a a normalization parameter, c a parameter related to the SD of the distribution, b a parameter related to its mean, and d an adjustable parameter.

The histogram can then be written as

$$h(z) = \Pi_1 G_{\mu,\sigma}(z) + \Pi_2 F_{b,c,d}(z), \qquad \text{[S7]}$$

with $p(C_1) = \Pi_1$, $p(C_2) = \Pi_2$, $p(z|C_1) = G_{\mu,\sigma}(z)$, and $p(z|C_2) = F_{b,c,d}(z)$.

Parameter estimation. Knowing the histogram of an image to be segmented, we can determine priors Π_1 and Π_2 and the parameters of the distributions by a least-squares fitting from Eq. **S7**. Once the parameters have been identified, the segmentation can be defined from the threshold obtained at the intersection of the two functions representing each term of Eq. **S7**.

Threshold. The position of the intersection is given immediately as an output of the adjustment process, with an accuracy of ±3 gray levels (green line in Fig. S5*C*). Along an experiment, i.e., considering all the images one by one, we found that the threshold calculated this way remains stable within ±2 levels of gray. Given this stability, we have chosen to use a fixed threshold for all images of the same experiment. This threshold is obtained as an average over all individual thresholds along the experiment. It is found to increase by about 10 gray levels as the normal load increases from 1 N to 6 N.

Fig. S5 *E* and *F* shows the results of the segmentation of images in Fig. S5 *A* and *B*, respectively, using the above-described method. White spots correspond to microjunctions. The great resemblance between the black spots of the image in Fig. S5*A* and the white spots in Fig. S5*E*, together with the quasi-absence of white spots in Fig. S5*F*, validates the adopted segmentation method. More quantitatively, if the image in Fig. S5*A* is segmented using the extremal values of the likelihood interval of the threshold over time (typically $X \pm 3.5$ with X around 50), we find that the relative variation on the contact area is lower than 7.7% between min and max.

Mean-Field Model Relating α_A and α_R. Greenwood and Williamson's model (13) describes a rough surface as a collection of independent spherical asperities, all with the same radius of curvature R and with a random height distribution with SD s. In the case of an exponential distribution, Baumberger and Caroli (18) observed that the average area of a microjunction is $\overline{A_0^{A,m}} = \pi R s$, independent on the normal load. As a consequence, the number of microjunctions involved in the multicontact grows linearly with the total area of real contact.

Based on these observations, we consider a mean-field model in which multicontacts are made of N identical, independent microjunctions of individual initial area $\overline{A_0^{A,m}}$, such that the initial macroscopic area of real contact is $A_0^R = N\overline{A_0^{A,m}}$. Based on the results of Fig. 2*C*, we further assume that, when the interface is sheared with a tangential force Q, each microjunction obeys a quadratic area reduction law of the form

$\overline{A^{A,m}} = \overline{A_0^{A,m}} - \alpha_A q^2$, with $q = Q/N$ and α_A the tangential load applied on and the area reduction parameter of each individual microjunction, respectively. Finally, based on the scaling law in Fig. 3, we also assume that $\alpha_A = \beta \overline{A_0^{A,m}}^\gamma$.

The macroscopic area reduction law will then be obtained by rewriting the expression $A^R = N \overline{A^{A,m}}$,

$$A^R = N \left(\overline{A_0^{A,m}} - \beta \overline{A_0^{A,m}}^\gamma q^2 \right) \qquad \text{[S8]}$$

$$= N \overline{A_0^{A,m}} - N \beta \overline{A_0^{A,m}}^\gamma \frac{Q^2}{N^2} \qquad \text{[S9]}$$

$$= A_0^R - \beta \frac{\overline{A_0^{A,m}}^\gamma}{N} Q^2 \qquad \text{[S10]}$$

$$= A_0^R - \beta \frac{\overline{A_0^{A,m}}^{\gamma+1}}{A_0^R} Q^2, \qquad \text{[S11]}$$

meaning that $\alpha_R = \beta_R \left(A_0^R \right)^{-1}$, with $\beta_R = \beta \overline{A_0^{A,m}}^{\gamma+1}$ being a constant independent of A_0^R (and of P). The obtained scaling ($\alpha_R \sim \left(A_0^R \right)^{-1}$) is in good agreement with the data shown in Fig. 3, *Inset*.

Reinterpretation of the Parameter B in the RSF Law. The Rice and Ruina formulation of the RSF law (23) is usually given as (18, 25, 26)

$$\mu(V, \theta) = \mu_0 + A \ln \left(\frac{V}{V_0} \right) + B \ln \left(\frac{V_0 \theta}{D_c} \right), \qquad \text{[S12]}$$

$$\dot{\theta} = 1 - \frac{V\theta}{D_c}, \qquad \text{[S13]}$$

with V the sliding velocity, V_0 an arbitrary reference velocity, D_c a critical slip length, and θ a state variable.

In the static case ($V = 0$), $\theta = t$, so for long hold times we have

$$\frac{d\mu_s}{d(\ln(t))} = B, \qquad \text{[S14]}$$

with $\mu_s = \frac{Q_s}{P} = \frac{\sigma A_s^R}{P}$ the static friction coefficient.

If one assumes that geometrical aging is the only mechanism involved in the selection of the area of real contact, Eq. **S14** could be integrated as

$$A_{s,aging}^R(t) = A_0^R + \frac{PB_{aging}}{\sigma} \ln(t). \qquad \text{[S15]}$$

Let us instead assume that after aging until time t, shear loading starts to be applied. The area of real contact of the aged interface, given by Eq. **S15**, corresponds to the initial area for the shear-induced reduction phenomenon. Assuming that shear loading is so fast that the additional geometrical aging is negligible during the time interval required to shear the interface from rest to the onset of sliding, Eq. **3** can be rewritten as

$$Q_s = \frac{1}{2\alpha_R \sigma} \left[\sqrt{1 + 4\alpha_R \sigma^2 \left(A_0^R + \frac{PB_{aging}}{\sigma} \ln(t) \right)} - 1 \right]. \qquad \text{[S16]}$$

Using Eq. **S14**, the parameter B can now be evaluated from the derivative of Q_S with respect to $\ln(t)$, which gives

$$B = \frac{1}{P} \frac{dQ_s}{d(\ln(t))} = \frac{B_{aging}}{\sqrt{1 + 4\alpha_R \sigma^2 \left(A_0^R + \frac{PB_{aging}}{\sigma} \ln(t) \right)}}. \qquad \text{[S17]}$$

Noting that $\sqrt{1 + 4\alpha_R \sigma^2 \left(A_0^R + \frac{PB_{aging}}{\sigma} \ln(t) \right)} = 1 + 2\alpha_R \sigma^2 A_s^R$ (replace Q_s with σA_s^R in Eq. **S16** and reorganize), we can rewrite Eq. **S17** as

$$B = \frac{B_{aging}}{1 + 2\alpha_R \sigma^2 A_s^R}. \qquad \text{[S18]}$$

Eq. **S18** directly shows that, due to shear-induced area reduction, B is always smaller than the value that one would expect (B_{aging}) if geometrical aging was the only mechanism at play. In other words, interpreting B as a direct quantifier of geometrical aging alone amounts to underestimating the rate of aging at the interface. To get a better sense of how much the underestimation is, remember that $\alpha_R \sigma^2 A_s^R$ corresponds to the relative area reduction due to shear (*Onset of Sliding* in main text). We have observed relative area reductions up to about 30%, so that the denominator of Eq. **S18** can be up to about 1.6, meaning that the rate of aging may be underestimated by up to about 40%.

Possible Implications of the Finite Optical Resolution of the Images. The optical resolution of any digital image is limited to the pixel lateral size s, typically 25 μm in our multicontact images. As a consequence, any structure of the area of real contact with a length-scale smaller than s cannot be resolved. This limitation may affect our measurements of A^R in two ways.

First, patches of real contact may contain holes that are out of contact and smaller than s^2. This effect would lead to an overestimation of A^R. To assess whether this case is frequent, we considered typical microjunctions and imaged them with different zoom magnitudes (see Fig. S6 for a typical example). When reducing the pixel size by a factor of 3 (maximum zoom available with our optical device), i.e., by reducing the pixel area by about one order of magnitude, we uncovered very few holes, so that the area measurement of microjunctions was virtually unaffected by the change of resolution. The fact that only few holes can be observed is qualitatively consistent with the low Young's modulus of PDMS which, under the action of adhesive stress, will easily deform to conform to the rigid substrate.

The second effect is that microjunctions with an area smaller than $A_{pix} = s^2$ have a low probability to be detected, leading to an underestimation of A^R. To quantify the missing area due to this effect, we characterized the probability density function (pdf) of the areas of individual microjunctions in unsheared interfaces, A_{0i}^A. We found that, for all normal loads, those pdfs are reasonably fitted by power laws, i.e., with a form $p(A_{0i}^A) = K(A_{0i}^A)^{-n}$. Assuming that this form is valid at all scales between 0 and the maximum microjunction size, $A_{0i,max}^A$, we can assess what the fraction is of the area that is constituted by microjunctions smaller than A_{pix}. The total area is given by

$$A_0^R = \int_0^{A_{0i,max}^A} A_{0i}^A p(A_{0i}^A) dA_{0i}^A = K \frac{(A_{0i,max}^A)^{2-n}}{2-n}, \qquad \text{[S19]}$$

while the area missed due to the finite size of the pixels is

$$A_{0,missed}^R = \int_0^{A_{pix}} A_{0i}^A p(A_{0i}^A) dA_{0i}^A = K \frac{(A_{pix})^{2-n}}{2-n}. \qquad \text{[S20]}$$

Finally, the fraction of missed area is $\frac{A_{0,missed}^R}{A_0^R} = \frac{(A_{pix})^{2-n}}{(A_{0i,max}^A)^{2-n}}$. With n found close to 1.5 and $A_{0i,max}^A$ being larger than $100\,A_{pix}$, we estimate that $\frac{A_{0,missed}^R}{A_0^R} \simeq \sqrt{\frac{A_{pix}}{A_{0i,max}^A}} < \frac{1}{10}$. This means that, in our experiments, the fraction of the area constituted by microjunctions smaller than the pixel size is always smaller than 10%

and is usually smaller than 5%. This fraction is of the order of or smaller than that associated to the uncertainty on A^R due to the determination of the segmentation threshold. Note that such an error is an absolute error and can affect the measured value of σ, by the same fraction. In contrast, the evolution of the area under shear relative to the initial area is essentially unaffected by this absolute error and thus does not affect the main conclusions of the present study.
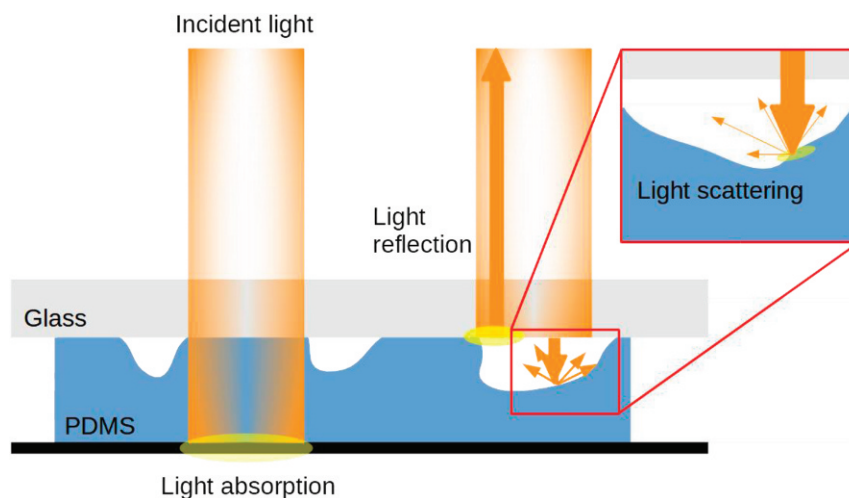

Fig. S1. Sketch of the light behavior at the interface. A rough PDMS sample (blue) in contact with a smooth glass plate (gray) is illuminated from the top by a diffuse white light. The light rays can be either transmitted through the real contact regions and absorbed by a black layer (bottom) or partly reflected by the glass/air dioptre and partly back scattered by the air/PDMS dioptre in out-of-contact regions.
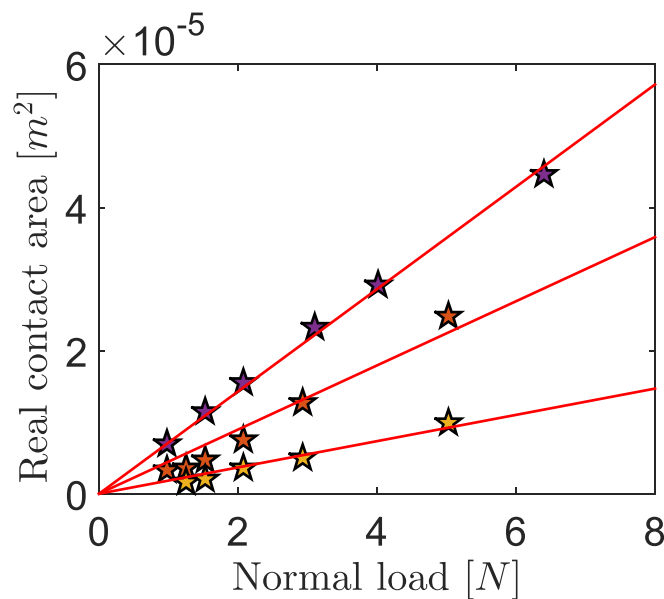

Fig. S2. Initial area of real contact is proportional to the normal load for multicontacts. Real contact area (for $Q = 0$) as a function of the normal load is shown. Purple: PDMS/glass multicontacts ($R_q = 26\ \mu$m). Orange: PDMS/cross-linked PDMS multicontacts ($R_q = 20\ \mu$m). Yellow: PDMS/grafted PDMS multicontacts ($R_q = 20\ \mu$m). Red lines: linear fits passing through the origin.
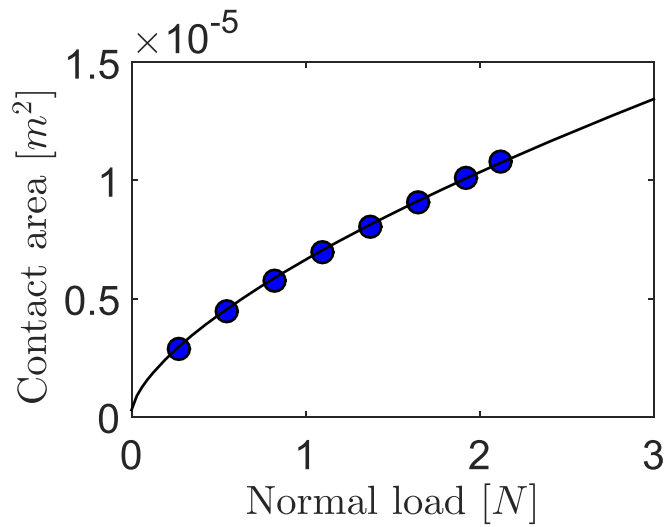
Fig. S3. Initial area of apparent contact is captured by the JKR model for sphere/plane contacts (43). Shown is apparent contact area (for $Q = 0$) as a function of the normal load, for the experiments shown in Fig. 2C. Solid line: prediction of the JKR model with $\nu = 0.5$, $w_0 = 27$ mJ/m^2, $R = 9.42$ mm, and $E = 1.9$ MPa. Note that, as mentioned in *Materials and Methods*, the value of w_0 was obtained separately using a dedicated apparatus.

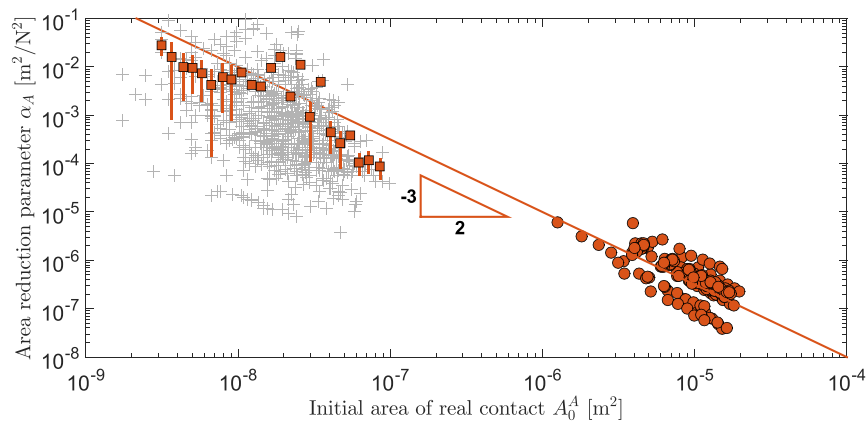**Fig. S4.** Area reduction across the scales. Shown is α_A as a function of A_0^A (PDMS/cross-linked PDMS type of interface, coating thickness 150 μm, $\sigma = 0.30 \pm 0.01$ MPa). Circles: sphere/plane contacts. $R = 9.42$ mm. $V = 0.1$ mm/s. Gray crosses: raw data for microjunctions within multicontacts. Squares: average of the raw data divided into 23 classes. Error bars: SD within each class. Solid line: guide for eyes with slope $-3/2$.
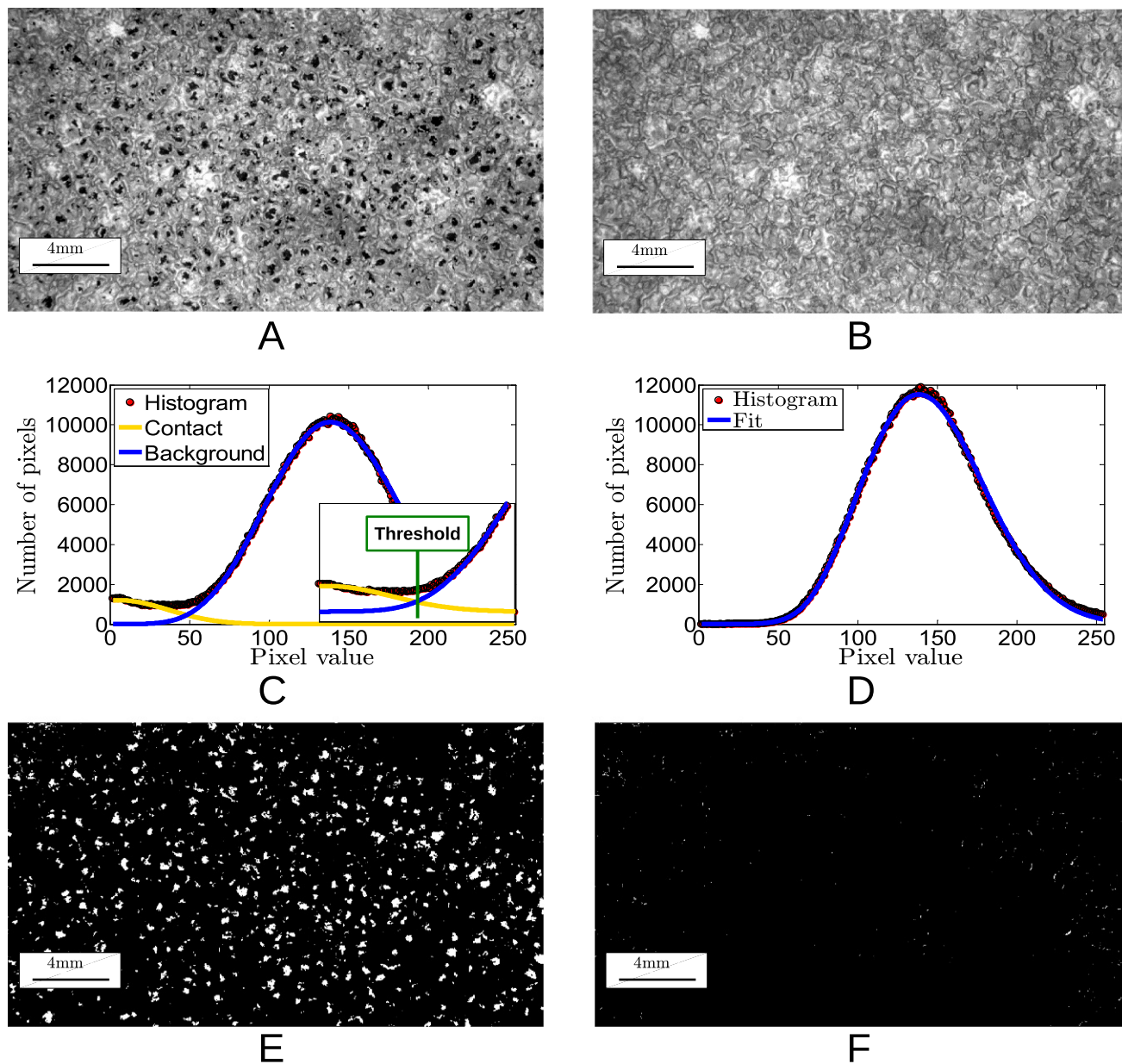
Fig. S5. Principle of the image segmentation. Shown is an example of a PDMS/glass multicontact, with $R_q = 26$ μm. (*A*) Raw contact image. (*B*) Raw non-contact image serving as a calibration for the shape of the out-of-contact histogram distribution. (*C*) Contact image histogram. (*D*) Out-of-contact image histogram. (*E*) Binarized contact image. (*F*) Binarized out-of-contact image.
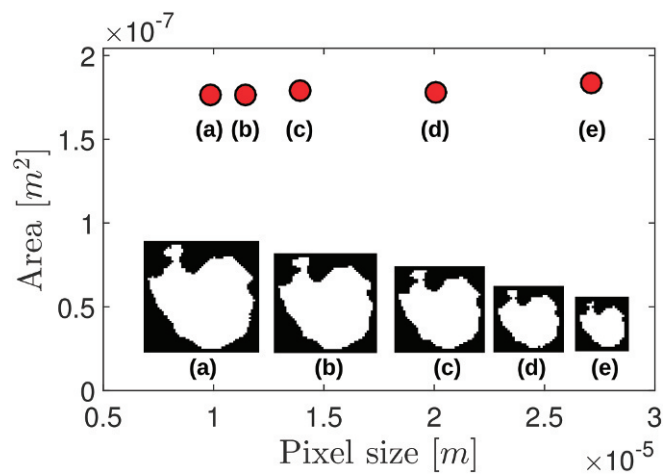
Fig. S6. Area measurements are essentially scale independent. Main plot (red circles) shows measured area of a microjunction as a function of the pixel size. Insets *a–e* show a segmented image of the same microjunction for various zoom-ins.